Interdisciplinary Research in Medical Sciences Specialty
ISSN: 3062-4401
2025, Volume 5, Issue 1, Page No: 189-211

Available online at: www.galaxypub.co/page/journals

Galaxy Publication

Light-Activated TROP2-Targeted Nanotheranostics Restore ADC Sensitivity and Induce Immunogenic Cell Death in TNBC

James Anderson[1], Maria Rossi[2]*, William Clark[3]

[1]Department of Nanomedicine and Cancer Therapeutics, Faculty of Pharmacy, University of Manchester, Manchester, United Kingdom.
[2]Department of Oncology and Immunogenic Cell Death, Faculty of Pharmacy, University of Milan, Milan, Italy.
[3]Department of Breast Cancer Research and Targeted Therapy, Faculty of Medicine, University of Melbourne, Melbourne, Australia.

***E-mail** ✉ maria.rossi@unimi.it

Received: 18 March 2025; **Revised:** 06 June 2025; **Accepted:** 08 June 2025

ABSTRACT

Chemoresistance together with immune evasion presents substantial barriers to effective therapy for triple-negative breast cancer (TNBC). These issues are intensified by the inadequate pharmacokinetic profiles and the emergence of resistance to antibody–drug conjugates (ADCs). Here, we report the design of antibody-directed nanoparticles (NPs) that simultaneously carry the TROP2-targeted ADC sacituzumab govitecan (SG) and the mitochondria-targeted near-infrared (NIR) photosensitizer AIE780. The constructed AIE780–SG nanoconjugates take advantage of hRS7 antibody guidance to achieve selective accumulation within TROP2-high, SG-resistant TNBC cells as well as patient-derived organoids. Under NIR light exposure, AIE780 provokes mitochondrial redox disruption by generating localized reactive oxygen species, thereby inducing tumor-specific immunogenic cell death (ICD) through membrane damage and oxidative necrotic pathways. Simultaneously, SG experiences acid-triggered cleavage that liberates SN-38, a highly active topoisomerase I inhibitor, along with the hRS7 antibody fragment that facilitates recruitment and stimulation of natural killer (NK) cells. In mouse models of TNBC xenografts, these AIE780–SG NPs demonstrated synergistic chemophotodynamic antitumor activity, successfully bypassing SG resistance and reinvigorating antitumor immune function. This light-responsive, TROP2-directed theranostic nanoplatform establishes a multimodal strategy to augment ADC performance and reshape the immunosuppressive milieu of TNBC, introducing an innovative approach for managing SG-resistant disease. A dual-action nanoplatform integrating targeted ADC delivery with photodynamic induction of ICD effectively circumvents SG resistance in TNBC while potentiating NK cell-driven antitumor immunity.

Keywords: Aggregation-induced emission, Photothermal therapy, Sacituzumab govitecan, Triple-negative breast cancer, Trophoblast cell-surface antigen 2

How to Cite This Article: Anderson J, Rossi M, Clark W. Light-Activated TROP2-Targeted Nanotheranostics Restore ADC Sensitivity and Induce Immunogenic Cell Death in TNBC. Interdiscip Res Med Sci Spec. 2025;5(1):189-211. https://doi.org/10.51847/pp6tUUtX6A

Introduction

Breast cancer persists as the leading malignancy in women, accounting for roughly 420,000 newly diagnosed cases in China during 2022 [1], and thus contributing significantly to the overall global cancer burden [2]. This upward trend in incidence arises not only from enhanced early detection enabled by broad screening efforts but also from the increasing adoption of westernized lifestyle patterns, such as altered dietary habits, postponed childbirth, and lower levels of physical activity [3]. Despite considerable progress in multimodal treatments—including surgical intervention, chemotherapy, targeted agents, and immunotherapy—the continued rise in breast cancer cases remains a pressing public health concern [4], highlighting the necessity for continued advancement in preventive measures, timely diagnosis, and tailored therapeutic regimens. Triple-negative breast cancer (TNBC), distinguished by the lack of estrogen receptor (ER), progesterone receptor (PR), and human epidermal

growth factor receptor 2 (HER2) expression, is recognized for its highly aggressive nature and unfavorable clinical outcomes [5].

Roughly 85%–90% of TNBC tumors exhibit elevated expression of trophoblast cell-surface antigen 2 (TROP2), positioning it as a compelling molecular target for therapy [6]. Sacituzumab govitecan (SG, IMMU-132), the pioneering antibody–drug conjugate (ADC) approved in the United States for TNBC, consists of a humanized anti-TROP2 monoclonal antibody (hRS7) conjugated to SN-38, the pharmacologically active metabolite of irinotecan that functions as a topoisomerase I inhibitor [7, 8]. SG has since been integrated into the 2022 Chinese clinical practice guidelines [9]. Nevertheless, a proportion of patients experience only modest therapeutic benefit due to poor tumor penetration, swift systemic elimination, and brief duration of action [10]. To overcome these constraints, various nanoplatforms have been developed to enhance SG's biodistribution and intratumoral retention, often combined with adjunctive approaches such as additional chemotherapy, phototherapy, or radiotherapy to bolster antitumor immune responses. Hence, an immediate priority exists for engineering advanced nanocarriers that harness features of the tumor microenvironment (TME) to promote greater SG accumulation and ensure a more potent, sustained therapeutic impact.

Photodynamic therapy (PDT) is experiencing renewed interest as a minimally invasive treatment option for breast cancer, valued for its strong safety characteristics, localized action, and ability to exert control in both time and space [11, 12]. PDT operates through photosensitizers (PSs) that, upon illumination with appropriate light, produce cytotoxic reactive oxygen species (ROS) capable of destroying malignant cells [13]. However, traditional PSs suffer from limitations including aggregation-caused quenching and photobleaching, which diminish ROS generation and compromise treatment outcomes [14]. In 2001, Luo *et al*. identified the contrasting process known as aggregation-induced emission (AIE), whereby molecular aggregation leads to amplified fluorescence and enhanced ROS production [15]. Concurrently, immunogenic cell death (ICD)—a specialized apoptotic process accompanied by the release of damage-associated molecular patterns (DAMPs), especially calreticulin (CRT) displayed on the cell surface—has gained prominence as a vital mechanism in cancer immunotherapy [16, 17]. ICD helps address the immunologically "cold" nature of tumors such as metastatic TNBC, thereby improving their responsiveness to immunotherapeutic strategies [18, 19]. A pivotal event in ICD is the relocation of CRT from the endoplasmic reticulum to the plasma membrane, where it serves as an "eat-me" signal that activates dendritic cells (DCs), supporting antigen presentation and the elicitation of adaptive antitumor immunity [20-23]. Earlier research produced AIE780 by means of a cationization method, granting it the capacity to generate type I reactive oxygen species (ROS) along with mitochondrial targeting properties [24]. Nonetheless, the selection of potent ICD inducers continues to be narrow. This limitation stems from the fact that planar photosensitizers (PSs) generally display low solubility, insufficient photostability, and reduced membrane affinity, which together result in inadequate ROS formation and weak ICD induction. Consequently, there remains a critical demand for the development of PSs possessing refined molecular designs capable of delivering strong ROS production, specific tumor antigen recognition, stability in aqueous media, and superior cellular uptake.

In this study, we present the preparation of AIE780-SG nanoparticles (NPs) that consist of an AIE780-COOH core linked to anti-TROP2. This dual-targeting nanoscale system merges ADC-driven tumor identification with AIE780-assisted organelle-directed transport, significantly improving tumor specificity and intracellular uptake within SG-resistant triple-negative breast cancer (TNBC). The incorporation of anti-TROP2 enables the NPs to localize to mitochondria, where they provoke mitochondria-dependent apoptosis by means of elevated ROS levels, mitochondrial dysfunction, and ICD stimulation. This process in turn mobilizes natural killer (NK) cell-driven antitumor immune responses, leading to successful suppression of primary tumor growth (Scheme 1). Additionally, AIE780-SG NPs exhibited superior performance in high-TROP2-expressing TNBC patient-derived organoids (PDOs), demonstrating their value as a systemic chemo-immunotherapeutic and theranostic platform.

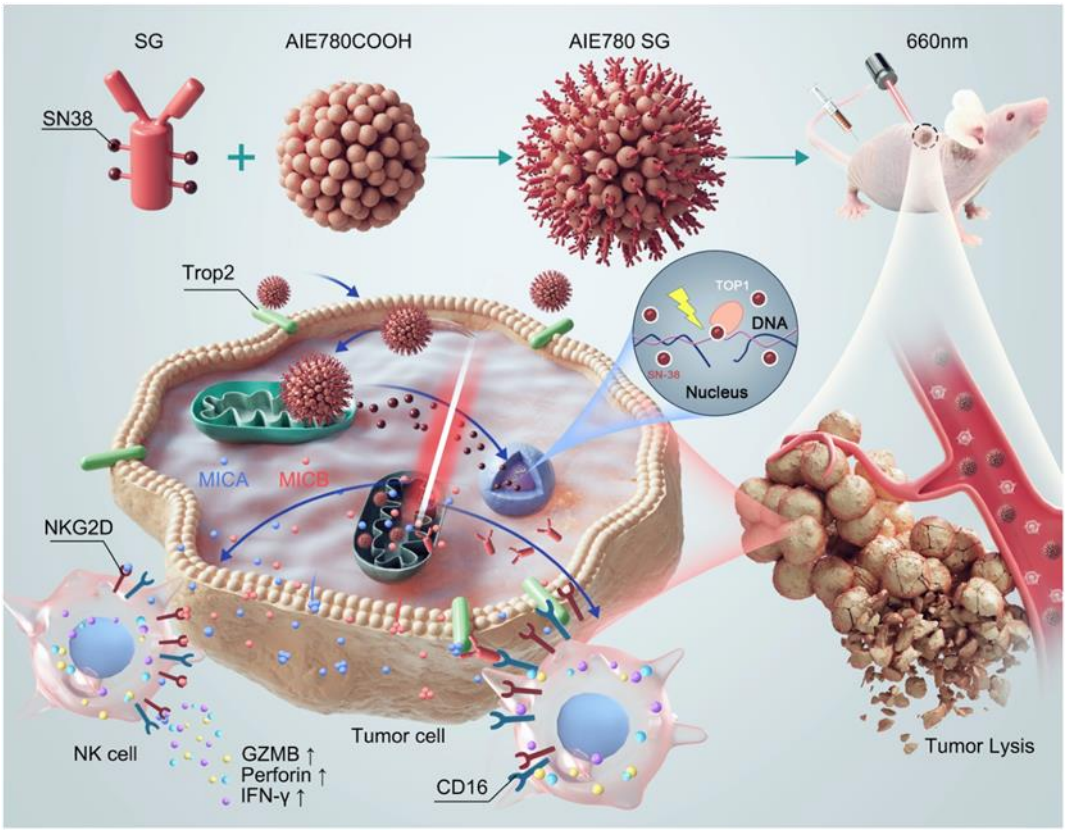

Scheme 1

Schematic representation of the fabrication of AIE780-SG NPs, the liberation of SG, and the approach for near-infrared fluorescence imaging (NIR FLI)-guided photo-enhanced chemotherapy against resistant TNBC cells. AIE780-SG contains the antibody component hRS7, which initially recognizes the TROP2 antigen displayed on the tumor cell surface. This binding promotes uptake of the complex into the cell and guides it to the mitochondria. After light exposure, MICA/B is liberated into the extracellular milieu, attracting numerous NK cells. MICA/B subsequently interacts with NKG2D receptors on these NK cells to promote their activation. Concurrently, the hRS7 antibody remains anchored on the tumor cell membrane and engages CD16 receptors on NK cells. This engagement induces the secretion of important cytotoxic effectors, such as granzyme B (GZMB), perforin, and interferon-γ (IFN-γ). These actions heighten the tumoricidal activity of NK cells. Moreover, the SG portion of AIE780-SG serves as an ADC that transports the chemotherapeutic payload SN38. This agent specifically interacts with topoisomerase I (TOP1) inside the nucleus, generating DNA strand breaks. The combined action reinforces antitumor immunity while inflicting direct DNA damage in tumor cells, thereby elevating overall treatment effectiveness. ADC, antibody–drug conjugate; FLI, fluorescence imaging; NIR, near-infrared; NK, natural killer; NPs, nanoparticles; SG, sacituzumab govitecan; TNBC, triple-negative breast cancer; TOP1, topoisomerase I; TROP2, trophoblast cell-surface antigen 2.

Materials and Methods

Preparation of AIE780-SG NPs

AIE780-SG NPs were synthesized following an adapted protocol reported in the literature. In short, 500 μg of AIE780-COOH dissolved in tetrahydrofuran (THF) was introduced into 9 mL of deionized water during sonication (SCIENTZ-II D, 80% power, 1 min). The organic solvent was subsequently removed by overnight stirring at 25°C. Following filtration (0.2 μm), 2 mL of the NP suspension was diluted to 8 mL with water and allowed to react with varying amounts of SG (250, 500, 1000, 2000, 2500 μg) in the presence of Sulfo-NHS (17.4 μg) and 1-ethyl-3-(3-dimethylaminopropyl)carbodiimide (EDC) (15.3 μg) at 25°C for 4 h. The resulting material was purified through centrifugation at 13,000 g to eliminate unbound substances, followed by two further washing-centrifugation steps using phosphate-buffered saline (PBS). The purified NPs were then resuspended in 8 mL of PBS to yield the stock solution. Following synthesis, bicinchoninic acid (BCA) protein quantification

assays were carried out on AIE780-SG samples prepared at different concentrations to quantify the actual antibody loading on the nanoparticle surface. Employing a BCA Protein Quantification Kit (Beyotime), the conjugated protein concentration was assessed in accordance with the manufacturer's microplate instructions. Briefly, 200 μL of working reagent was combined with 20 μL of bovine serum albumin (BSA) standards (0–500 μg/mL range) in a 96-well plate and mixed well. The plate was incubated at 37°C for 30 min, after which absorbance was recorded at 562 nm with a Spectrostar Nano microplate reader to generate a calibration curve. The identical protocol was then performed with the AIE780-SG samples to calculate antibody concentration from the calibration curve.

Characterization of AIE780-SG NPs

Particle size and zeta potential of AIE780 NPs and AIE780-SG NPs were determined at 25°C with a Zeta Plus Potential Analyzer (Brookhaven Instruments Corporation). The morphology of IT-PEG-RGD NPs was visualized using a transmission electron microscope (TEM; FEI Tecnai TEM) operating at 120 kV. Fluorescence spectra of AIE780-SG NPs were obtained on a Horiba Fluorolog-3 spectrofluorometer with a quartz cuvette.

Cell culture

Five human breast cancer cell lines—MCF10A, MDA-MB-231, Hs578T, BT549, and BT-20—as well as the murine breast cancer cell line 4T1 were acquired from Zhejiang Meisen Cell Technology Co., Ltd (Hangzhou, China). These cells were routinely maintained in Dulbecco's modified Eagle medium (DMEM; Gibco) supplemented with 10% fetal bovine serum (ExCell Bio, FSP500). BT-20 cells were grown in their designated medium (CM-0324; Wuhan Procell Life Science and Technology Co. Ltd.). Standard incubation conditions for all lines consisted of a humidified environment at 37°C containing 5% CO_2 and 95% air.

In vitro cellular uptake of AIE780-SG and intracellular ROS detection

Prior to experiments, TNBC cells were kept in the logarithmic growth phase via routine subculturing. Cells were plated at 5×10^4 cells per dish in glass-bottom confocal dishes and allowed to attach for 24 h. The medium was then exchanged for fresh complete medium containing AIE780-SG NPs (corresponding to 5 μM AIE780). After an additional 14 h, the cells were co-incubated with Mitotracker Green (200 nM) for 30 min.

Intracellular ROS levels were monitored using 2′,7′-dichlorodihydrofluorescein diacetate (DCFH-DA) as a fluorescent indicator. Following 24 h culture in glass-bottom confocal dishes, the medium was replaced with complete medium containing either free AIE780 (5 μM) or AIE780-SG NPs (5 μM). After 4 h incubation, DCFH-DA was introduced. Thirty minutes later, the cells were rinsed twice with PBS and subjected to white light irradiation (2.0 W cm^{-2}) for 5 min before imaging via confocal laser scanning microscopy.

For flow cytometry (FCM) assessment of ROS generation, BT-20 cells were seeded into 6-well plates. After 24 h, cells were allocated to treatment groups: PBS, SG, AIE780, AIE780 + Laser, AIE780-SG, and AIE780-SG + Laser (all at 5 μM). Following the respective treatments, cells were harvested, resuspended in 10 μM DCFH-DA, and incubated at 37°C for 30 min. Excess extracellular probe was removed by washing, after which ROS production was quantified by FCM.

CCK-8 assay

IC_{50} determination for SG in cells and organoids: Cells and TNBC-PDOs were exposed to a range of SG concentrations (0.032, 0.16, 0.8, 4, 20, 100 μM), washed with PBS, and then either kept in the dark or irradiated with white light for 30 min. Cell viability relative to untreated controls was evaluated using the standard CCK-8 method.

Evaluation of cell viability under different treatment conditions: Cells were treated with PBS, AIE780, or AIE780-SG NPs at concentrations of 0, 0.3125, 0.625, 1.25, 2.5, and 5 μM. After PBS washing, samples were either maintained in the dark or exposed to white light irradiation for 10 min. Viability was subsequently measured by the standard CCK-8 assay relative to untreated cells.

FCM detection of apoptosis

Cells were treated with 5 μM SG, 5 μM AIE780, or 5 μM AIE780-SG NPs, washed with PBS, and subjected to white light irradiation (2.0 W cm^{-2}) or kept in the dark for 10 min. Apoptosis rates and organoid damage were quantified using Annexin V-FITC/PI staining.

Immunofluorescence experiment for CRT

BT-20 cells were seeded in confocal dishes and, after 24 h, assigned to the following treatment groups: PBS, SG, AIE780, AIE780 + Laser, AIE780-SG, and AIE780-SG + Laser. Following treatment, samples were fixed with 4% paraformaldehyde for 10 min, rinsed with PBS, and permeabilized using 0.2% Triton X-100 for 5 min. Nonspecific binding was blocked with 5% goat serum at room temperature for 1 h. Samples were then incubated with anti-CRT primary antibody (1:200 dilution) at 4°C overnight (12 h). After PBS washes, secondary antibody was applied for 1.5 h at room temperature. The specimens were washed again, mounted with anti-fade medium containing DAPI, and imaged by confocal microscopy. Mean fluorescence intensity was determined for analysis.

ELISA detection of adenosine triphosphate (ATP)

Standard working solution or cell culture supernatant from BT-20 cells was added to the designated wells of the ELISA plate. Subsequently, 100 μL of HRP-conjugated antibody working solution was added to each well, followed by incubation at 37°C for 60 min. After discarding the contents and washing the plate five times, 100 μL of substrate mixture (A and B combined at a 1:1 ratio) was dispensed into each well. The plate was incubated in the dark at 37°C for 15 min. The reaction was terminated by adding 50 μL of stop solution per well, and the optical density was immediately recorded at 450 nm for data processing.

Establishment of three-dimensional patient-derived organoid models

Organoids consist of clusters of adult stem cells or pluripotent stem cells that are cultured in three-dimensional conditions in vitro, enabling them to reorganize into miniature structures that mimic organ-specific functions [25, 26]. TNBC tissue samples were obtained from patients undergoing surgery at the Department of Breast and Thyroid Surgery, Southwest Hospital, Army Medical University. This study was reviewed and approved by the Research and Clinical Experiment Ethics Committee of the Army Medical University (No. 2023-KY-0484). Specialized breast cancer organoid culture medium (PRS-BCM-3D) for TNBC-PDOs was acquired from Precedo Biotech Co., Ltd. For PDO establishment, freshly excised tumor tissue was rapidly transferred into DMEM containing 2% penicillin/streptomycin. The tissue was minced into thin slices of about 1 mm thickness and then enzymatically digested using DMEM/F12 medium supplemented with 3 mg/mL type I and type IV collagenase at 37°C for 1 h. After digestion, the cell suspension was passed through a 70-μm filter and washed twice with culture medium. Around 15,000 cells combined with 30 μL Matrigel were seeded into each well of 24-well plates. The plates were inverted and incubated at 37°C for 0.5 h to promote gel solidification. Once the Matrigel had hardened, 500 μL of organoid culture medium was added per well, with medium changes performed every 2 days over a period of approximately 1 week.

TNBC-PDOs viability assay

Susceptibility of TNBC-PDOs to SG was assessed through viability testing. Organoids were first dissociated with TrypLE Express (Gibco, 12605028) and then embedded in Matrigel at 2000 cells per well in 96-well plates (using 4 μL Matrigel per well). Following 7 days of growth, the organoids were exposed to SG concentrations of 0, 0.032, 0.16, 0.8, 4, 20, and 100 μM for 6 days. Bright-field images of the entire 96-well plate were captured with a microscope. The PDO spheres were subsequently dissociated, and a 100 μL portion was collected for measurement using the Cell Counting-Lite 3D Cell Viability Assay (DD112-02, Vazyme Biotech). The assay reagent was thawed at room temperature beforehand. A 100 μL aliquot of the organoid suspension was transferred to wells of a white opaque 96-well plate (BS-MP-96W, Biosharp), after which an equal volume of the reagent was added. The plate contents were mixed vigorously on a shaker for 5 min to ensure complete lysis. After an additional 30 min incubation at room temperature for signal stabilization, luminescence was recorded.

Internalization of AIE780-SG NPs and apoptosis level detection in TNBC-PDOs

When TNBC-PDOs had developed to a sufficient size, they were harvested and the Matrigel matrix was removed with Cell Recovery Solution (Corning, 354253). Then, 100 μL of PBS containing AIE780 or AIE780-SG NPs was introduced. Mitochondria and nuclei were labeled for 20 min using mitochondrion-selective MitoFluor™ dye and DAPI (Sigma-Aldrich), respectively. Real-time uptake and distribution of AIE780-SG NPs within the organoids were observed with a benchtop spinning disk confocal microscope (Oxford Instruments) in Z-stack mode. For apoptosis evaluation in TNBC-PDOs by confocal imaging, organoids were treated with PBS, 5 μM SG, 5 μM AIE780, or 5 μM AIE780-SG NPs, rinsed with PBS, and exposed or not exposed to white light

irradiation (2.0 W cm^{-2}) for 10 min. Apoptosis was detected and quantified using the Annexin V-FITC/PI kit as specified by the manufacturer, followed by fluorescence microscopic examination.

Animal models

Female BALB/c nude mice aged 4–5 weeks were subcutaneously inoculated in the right flank with 1×10^6 BT-20 cells suspended in 100 μL PBS. Seven days later, when tumor volumes had grown to approximately 100 mm^3, animals were either used for in vivo near-infrared (NIR) fluorescence imaging (FLI) studies or stratified into six experimental groups (n = 5 mice per group): PBS, SG, AIE780, AIE780 + Laser, AIE780-SG, and AIE780-SG + Laser. On days 7 and 14, mice received tail vein injections of 12.5 μM SG or AIE780-SG at a volume of 5 μL per gram body weight. Laser irradiation (660 nm for 5 min) was administered 6 h after NP injection in the appropriate groups. Tumor temperature during irradiation was continuously monitored using an infrared thermal imaging camera and maintained under 50°C. The treatment cycle was repeated one week later. Tumor dimensions and mouse body weights were measured every other day, with tumor volume computed according to the formula $V = (\text{length} \times \text{width}^2)/2$. All mice were euthanized on day 21 after inoculation for subsequent blood and organ analyses.

Histological analysis of mouse tumors

Major organs along with selected tumor tissues were fixed in 4% paraformaldehyde. Sections were prepared for hematoxylin and eosin (H&E) staining and for immunohistochemistry (IHC) targeting Ki-67 to determine tumor cell proliferative activity. Additional tumor sections underwent immunofluorescence staining for TUNEL, HIF1α, CD31, and murine NK cell markers (CD49b and NKG2D).

Cytological analysis of mouse tumors

Tumor tissues were processed to obtain single-cell suspensions. NK cell infiltration was evaluated by flow cytometry applying a $CD45^+CD3^-CD49b^+$ gating strategy. Intracellular cytokine profiling of tumor-infiltrating lymphocytes involved fixation and permeabilization using the appropriate staining kit protocol, followed by labeling with anti-mouse Granzyme B-PECy7, anti-Perforin-APC-Cy7, and anti-IFN-γ-V450 antibodies. Stained cells were analyzed immediately by FCM.

Hematological analysis of mouse

Peripheral blood was collected from mice in each treatment group to assess liver and kidney function parameters. Serum concentrations of Granzyme B (BYabscience, BY-EM220455), Perforin (BYabscience, BY-EM220230), and interferon-γ (IFN-γ) (BYabscience, BY-EM220140) were additionally quantified by ELISA kits according to the supplied protocols.

The activation detection of DC cells

Bone marrow-derived dendritic cells (DCs) were obtained from BALB/c nude mice and differentiated over 7 days in Roswell Park Memorial Institute (RPMI) 1640 medium supplemented with 20 ng/mL granulocyte-macrophage colony-stimulating factor (GM-CSF) and 10 ng/mL IL-4. Once differentiated, the cells were assigned to six experimental conditions: PBS, SG, AIE780, AIE780 + Laser, AIE780-SG, and AIE780-SG + Laser (5 μM, 2.0 W cm^{-2} where indicated). Twelve hours post-treatment, flow cytometry (FCM) was utilized to evaluate surface marker expression of CD86, CD80, and major histocompatibility complex class II (MHC-II), thereby determining the extent of DC activation.

Cytotoxicity and antibody-dependent cell-mediated cytotoxicity (ADCC) assays

NK cells were extracted from the spleens of nude mice with the EasySep™ Mouse NK Cell Isolation Kit prior to functional testing. Cytotoxic activity of NK cells was examined in a 6-hour flow cytometry protocol. Tumor cells pre-stained with Cell Tracker CM-DiI Dye were cultured overnight before being co-incubated with NK cells at effector-to-target ratios of 2:1 and 4:1. Following 4 hours of co-culture, tumor cell death was quantified using the Live/Dead Fixable V500-Aqua Dead Cell Staining Kit (Thermo Fisher), and NK cell degranulation was assessed via CD107a surface expression. Measurements were acquired on a Canto II flow cytometer (BD Biosciences) and processed using FlowJo software version 10.

Western blotting

BT-20 cells were plated at 1×10^4 cells per well in 6-well plates and allowed to settle for 12 h. Cells were then treated with 5 μM SG, 5 μM AIE780 NPs, or 5 μM AIE780-SG NPs, rinsed with PBS, and irradiated with white light (2.0 W cm^{-2}) for 10 min. After an additional 12 h, cells were lysed in radioimmunoprecipitation assay (RIPA) buffer (Thermo Scientific). Protein concentrations were measured by BCA assay (Thermo Scientific). Samples containing 20 μg of total protein were separated by SDS-PAGE electrophoresis and transferred to PVDF membranes (Millipore). Membranes were blocked in 5% skim milk dissolved in 1× TBST for 60 min at room temperature, followed by overnight incubation at 4°C with primary antibodies in 1× TBST containing 5% BSA. After five washes with 1× TBST, HRP-linked secondary antibodies were applied for 2 h at room temperature. Blots were washed three times with PBS and developed with enhanced chemiluminescence (ECL) substrate (Thermo Scientific) on a Bio-Rad imaging system. Densitometric analysis of protein bands was conducted with ImageJ software.

Statistical analysis

Data analysis was carried out using SPSS version 25. All experimental groups contained at least five biological replicates ($n \geq 5$). Comparisons of treatment efficacy were performed by one-way or two-way analysis of variance (ANOVA). Post-hoc two-sided least significant difference (LSD) tests identified statistically meaningful differences between groups. Levels of significance were indicated as: ns (not significant), $p > .05$, $*p > .05$, $**p < .01$, $***p < .001$, $****p < .0001$.

Results and Discussion

Molecular design, synthesis and photophysical properties of AIE780-SG NPs

Designing photosensitizers (PSs) capable of robust ROS generation while maintaining high aqueous dispersibility and efficient cellular penetration to drive strong immunogenic cell death (ICD) in TNBC remains technically demanding [27]. To address these constraints, the humanized anti-TROP2 antibody hRS7 was linked to AIE780 NPs, producing the AIE780-SG nanoconjugate. During formulation optimization, surface-bound protein levels on AIE780 NPs were quantified using the micro-BCA assay across SG concentrations ranging from 0 to 500 μg/mL, revealing conjugation efficiencies between 39% and 85%. After evaluating both binding efficiency and total antibody payload, a concentration of 62.5 μg/mL SG (500 μg SG combined with 500 μg AIE780 in 8 mL) was selected for all further experiments, achieving approximately 70% conjugation efficiency. Characterization by dynamic light scattering (DLS) and transmission electron microscopy (TEM) **(Figures 1a and 1b)** showed hydrodynamic diameters of 94.73 ± 1.37 nm for plain AIE780 NPs and 113.24 ± 2.10 nm for AIE780-SG NPs. These dimensions are favorable for prolonged systemic circulation and passive tumor targeting through the enhanced permeability and retention (EPR) effect [28, 29]. Although antibody attachment altered particle morphology to some extent, it did not promote aggregation or sedimentation, preserving dispersion stability appropriate for nanotherapeutic use **(Figure 1c)**. Absorption spectra in PBS exhibited maxima at 605 nm and 635 nm for AIE780 and AIE780-SG, respectively **(Figure 1d)**. Exposure to 660 nm NIR light at 2.0 W cm^{-2} caused AIE780-SG NPs to reach 45°C within 2 minutes **(Figures 1e and 1f)**. The conjugated nanoparticles displayed consistent photothermal performance comparable to unmodified AIE780 NPs, with no substantial decline after fabrication **(Figure 1g)**. Temperature elevation scaled proportionally with both laser power and nanoparticle concentration **(Figures 1h and 1i)**. Controlled release experiments indicated that roughly 30% of SG was liberated in serum-free PBS, whereas release remained limited to around 10% in the presence of serum, supporting adequate stability during blood transport and reduced nonspecific leakage **(Figure 1j)**. Release was markedly accelerated under low pH and elevated temperature conditions that simulate the tumor milieu **(Figures 1k and 1l)**. Overall, the hRS7-functionalized AIE780-SG platform successfully integrates EPR-compatible size, reliable photothermal properties, and environment-responsive drug liberation, thereby overcoming major limitations in the application of ROS-based ICD strategies for TNBC.

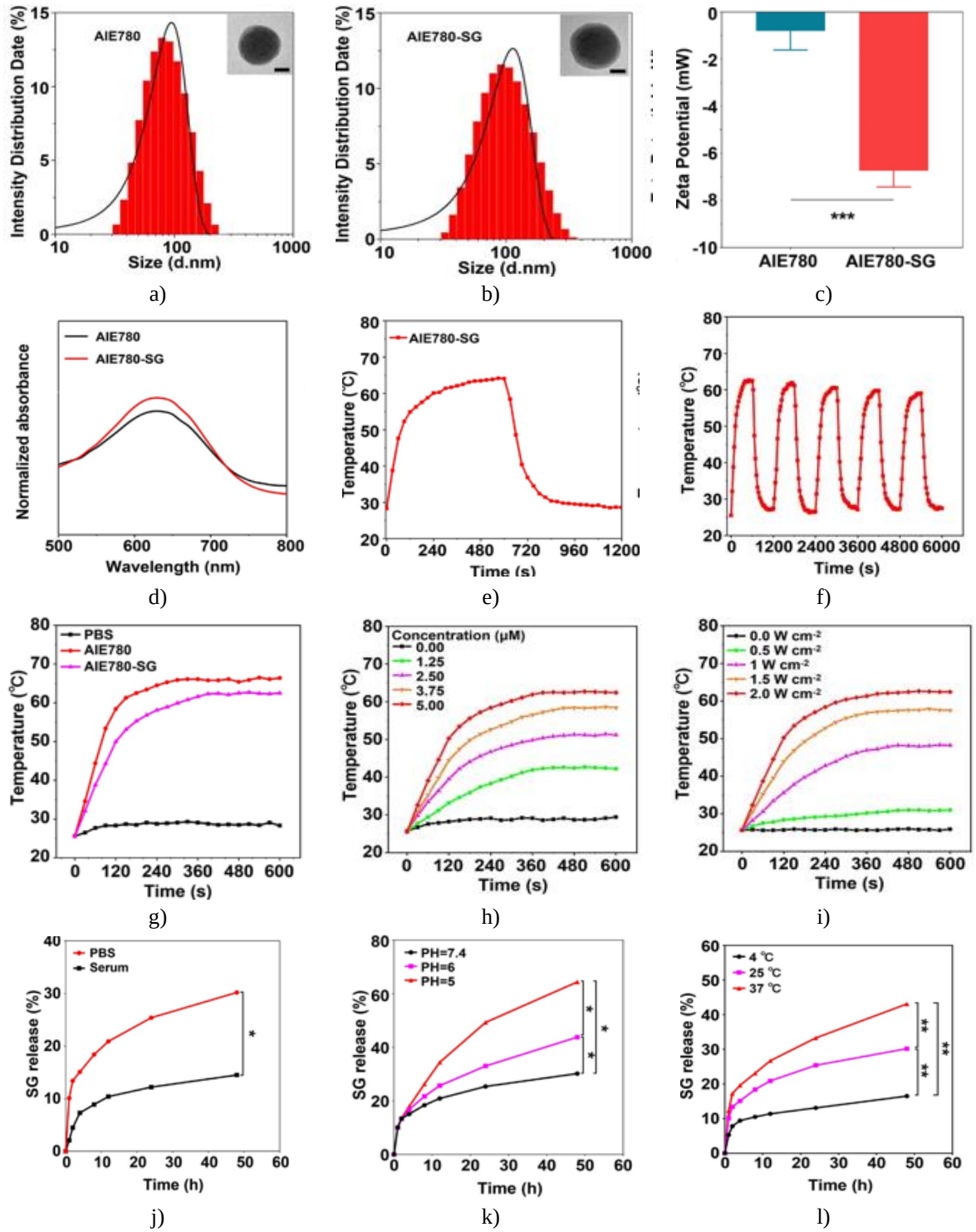

Figure 1. Photophysical performance of AIE780 and AIE780-SG NPs.
(a and b) Hydrodynamic size distributions and representative TEM micrographs of AIE780 and AIE780-SG NPs (scale bars in insets: 40 nm). (c) Zeta potential profiles of AIE780 and AIE780-SG. (d) UV-vis absorption spectra recorded in PBS (c = 5 μM, λex = 660 nm). (e) Time-dependent temperature increase of AIE780-SG nanoparticles upon NIR irradiation (c = 5 μM, 2 W cm^{-2}). (f) Cyclic photothermal stability test of AIE780-SG showing temperature profiles during repeated laser on/off cycles (2 W cm^{-2}, total 10 min, c = 5 μM). (g) Comparative heating curves for PBS, AIE780, and AIE780-SG under 660 nm laser exposure (2.0 W cm^{-2} for 10 min, c = 5 μM). (h, i) Photothermal heating as a function of nanoparticle concentration (at 2.0 W cm^{-2}) and laser power density (at c = 5 μM). (j) Cumulative SG release profiles from AIE780-SG in PBS versus serum-containing buffer. (k and l) Influence of pH and temperature on SG release kinetics from

AIE780-SG. AIE, aggregation-induced emission; NPs, nanoparticles; SG, sacituzumab govitecan; PBS, phosphate buffer saline; TEM, transmission electron microscope. *$p < .05$; **$p < .01$; ***$p < .001$.

In vitro tumor cell imaging and subcellular localization using AIE780-SG NPs

Antibody-drug conjugates like SG are engineered to preferentially recognize cells that overexpress TROP2 on their surface. The therapeutic success of AIE780-SG hinges on its capacity for efficient internalization. Given the inherent SG resistance of BT-20 cells, studies were performed to ascertain whether the nanoconjugate could circumvent this limitation in TNBC models. Protein expression analysis by western blotting combined with flow cytometry **(Figures 2a–2c)** confirmed markedly upregulated TROP2 in BT-20 cells relative to MCF-10A epithelial controls. Cell viability testing in a panel of TNBC lines further revealed that high-TROP2-expressing cells, most notably BT-20, displayed considerable resistance toward SG when administered alone **(Figure 2d)**. Confocal fluorescence microscopy showed clear penetration of AIE780-SG NPs across the plasma membrane and subsequent accumulation in mitochondria, where intense red emission overlapped with nuclear DAPI and mitochondrial MitoTracker Green labeling **(Figure 2e)**. By contrast, low-TROP2 MCF-10A cells demonstrated negligible nanoparticle internalization. Dynamic live-cell imaging illustrated progressive uptake and mitochondrial trafficking of AIE780-SG NPs in BT-20 cells within 4 h **(Figure 2f)**. These results indicate that AIE780-SG capitalizes on tumor-specific TROP2 overexpression for selective uptake and accurate mitochondrial delivery. Through hRS7-driven targeting, AIE780-SG achieves preferential engagement of TROP2-overexpressing TNBC cells, effectively bypasses SG resistance, and attains mitochondrial localization, as corroborated by expression profiling, pharmacological sensitivity data, and real-time visualization.

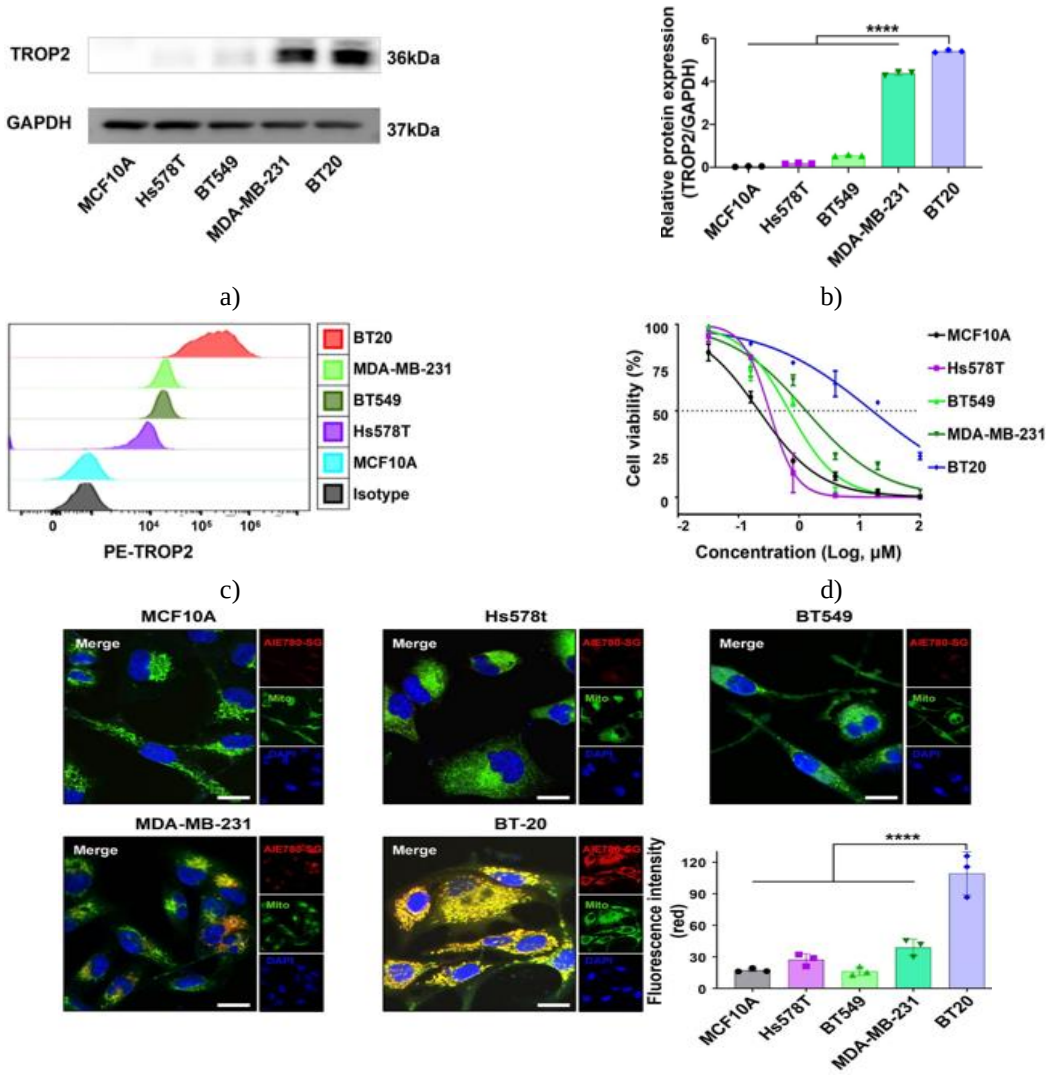

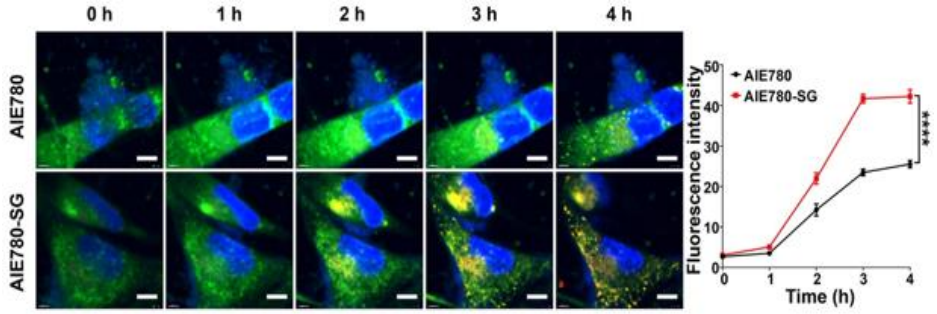

f)

Figure 2. Evaluation of TROP2 levels and SG responsiveness in multiple TNBC cell lines along with intracellular trafficking patterns of AIE780-SG NPs and their association with mitochondria. (a) Western blot images depicting TROP2 protein abundance in assorted breast cancer cell lines. (b) Densitometry-based quantification of TROP2 expression across the tested breast cancer cell lines. (c) Flow cytometry histograms illustrating TROP2 surface expression in various breast cancer cell lines. (d) Concentration-response curves showing SG IC50 values for different breast cancer cell lines. (e) Representative images of AIE780-SG NP distribution in breast cancer cell lines and corresponding quantitative colocalization analysis with mitochondria. Scale bar: 20 μm. (f) Time-course imaging of AIE780 versus AIE780-SG NP localization and mitochondrial overlap in BT-20 cells at successive time points post-incubation. Scale bar: 5 μm. FCM, flow cytometry; SG, sacituzumab govitecan; TNBC, triple-negative breast cancer; TROP2, trophoblast cell-surface antigen 2. ****$p < .0001$.

In vitro intracellular ROS generation, apoptotic induction, and DNA damage by AIE780-SG NPs

Earlier observations established predominant mitochondrial localization of AIE780-SG NPs as the basis for its cytotoxic activity. Subsequent work examined resulting changes in mitochondrial fine structure. Bio-TEM examination disclosed extensive organelle injury in cells exposed to AIE780-SG combined with laser exposure, featuring disrupted membranes, loss of cristae architecture, organelle condensation, and overall shrinkage—typical morphological signs of controlled cell death pathways **(Figure 3a)**. Generation of intracellular ROS was monitored with the DCFH-DA fluorescent indicator [30]. Both confocal imaging and flow cytometric measurements demonstrated significantly augmented ROS production in BT-20 cells under AIE780-SG + Laser conditions compared with other treatments **(Figures 3b and 3c)**.

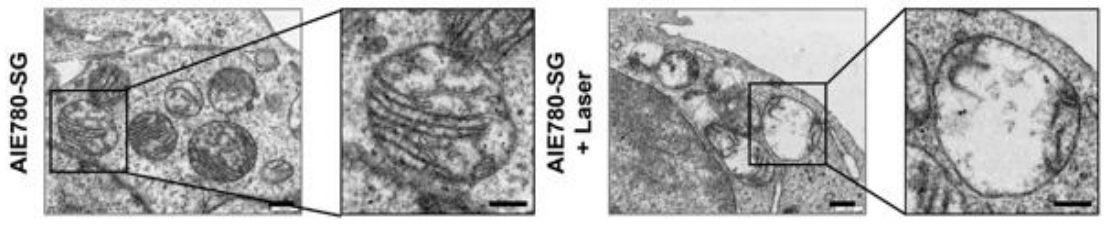

a)

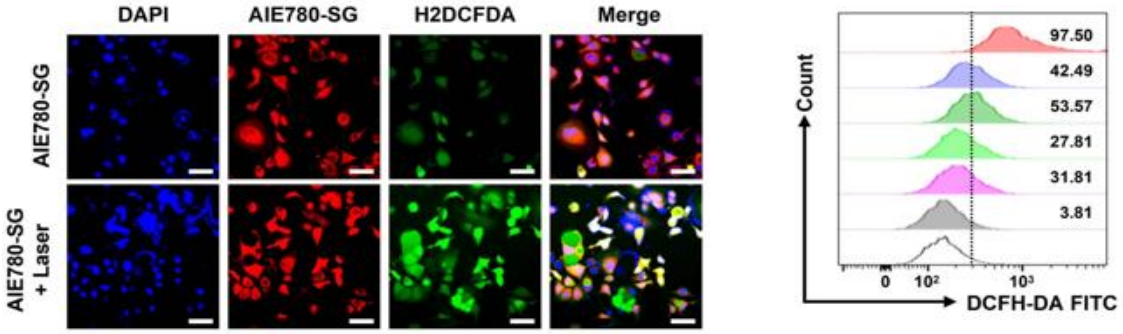

b) c)

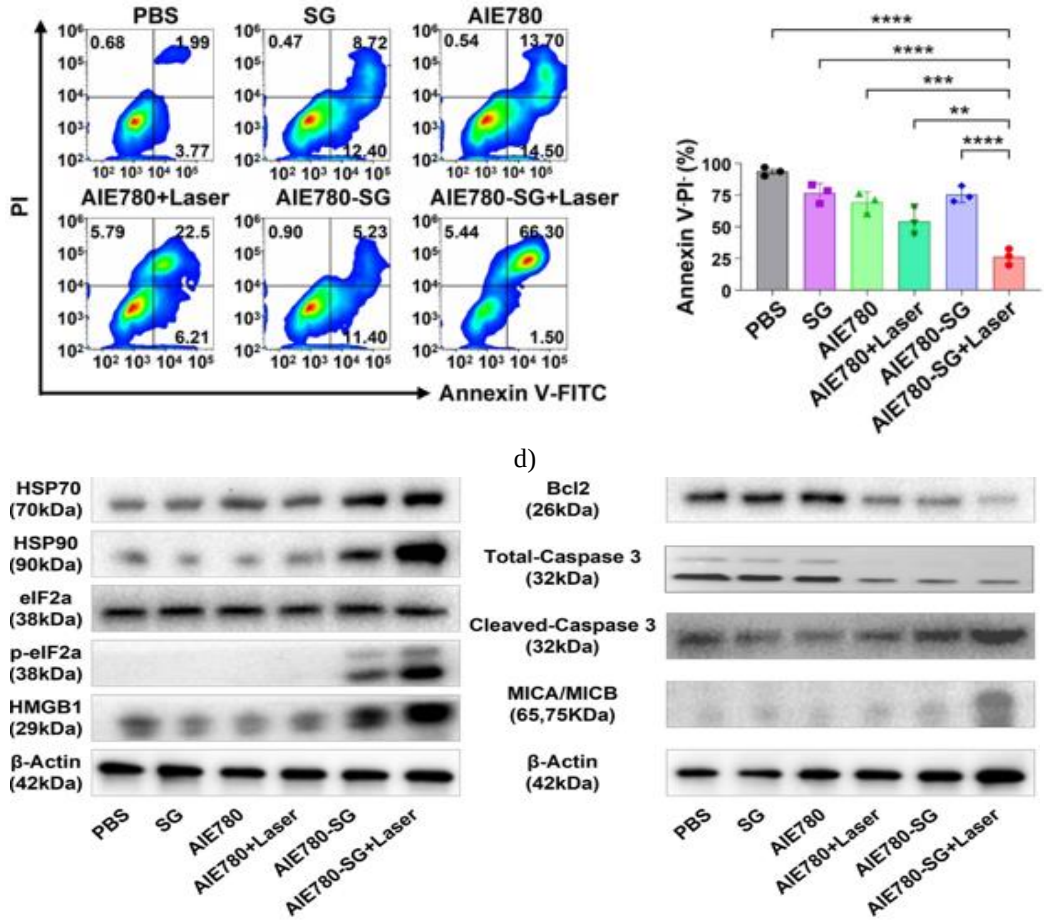

Figure 3. Influence of AIE780 and AIE780-SG NPs upon mitochondrial architecture, ROS levels in BT-20 cells, apoptotic induction, and expression profiles of key regulatory proteins following diverse interventions. (a) Transmission electron microscopy views of mitochondrial ultrastructure in BT-20 cells after AIE780-SG treatment with or without 660 nm laser application, accompanied by magnified insets to highlight specific damage features. Scale bar: 500 nm (overview), 200 nm (enlarged). (b) Fluorescence imaging of ROS in BT-20 cells using H2DCFDA probe following AIE780-SG exposure with or without 660 nm laser irradiation. Scale bar: 50 μm. (c) Flow cytometric detection of ROS generation in BT-20 cells labeled with DCFH-DA (overlaid histograms ordered from bottom to top: Isotype, PBS, SG, AIE780, AIE780 + Laser, AIE780-SG, AIE780-SG + Laser). (d) Representative flow cytometry plots quantifying apoptosis in BT-20 cells. Annexin V+ PI− (Q4 quadrant) corresponds to early apoptosis, Annexin V+ PI+ (Q2) to late apoptosis, and Annexin V− PI− (Q1) to viable cells. (e) Immunoblot images displaying expression of apoptosis-associated proteins (HSP70/HSP90, p-eIF2α/eIF2α, Bcl2, Total-Caspase3, Cleaved-Caspase3, and MICA/MICB) across treatment conditions in BT-20 cells. Results are expressed as mean percentages derived from three independent experiments conducted in duplicate (n = 3). DCFH-DA, 2′,7′-dichlorodihydrofluorescein diacetate; FCM, flow cytometry; NPs, nanoparticles; PBS, phosphate buffer saline; ROS, reactive oxygen species; SG, sacituzumab govitecan. ***p* < .01; ****p* < .001; *****p* < .0001.

Of note, standalone SG treatment produced little evidence of synergistic killing, while the AIE780-SG + Laser regimen triggered robust cell death, emphasizing the benefit of integrated nanoparticle delivery in surmounting resistance in TNBC. In addition, γH2AX foci formation, indicative of DNA double-strand breaks, was prominently increased following AIE780-SG + Laser exposure, consistent with enhanced genotoxic effects from photo-activated SN-38 liberation [31]. In summary, these results show that AIE780-SG NPs successfully merge photodynamic ROS generation with chemotherapeutic action to achieve enhanced tumor cell killing with potentially reduced systemic adverse effects.

AIE780-SG nanoparticles selectively target and synergistically bypass SG resistance in TNBC patient-derived organoid models

To provide additional confirmation of the precise targeting capability of AIE780-SG, TNBC patient-derived organoids (TNBC-PDOs) were employed. These three-dimensional culture systems accurately mirror the native tumor microenvironment and represent a critical platform for precision oncology, high-throughput drug evaluation, and investigations into tumor-immune interactions. TNBC-PDOs were generated and subsequently classified into SG-sensitive and SG-resistant subgroups **(Figures 4a and 4b)**. Histological examination via H&E staining, together with TROP2 immunohistochemistry, verified the reliable establishment of SG-resistant TNBC-PDOs (TNBC-PDO-R) **(Figures 4c and 4d)**. Following exposure to AIE780-SG nanoparticles, the resistant organoids displayed considerably stronger red fluorescence signals than those incubated with AIE780 alone, confirming preferential uptake and retention of the targeted nanoparticles **(Figure 4e)**.

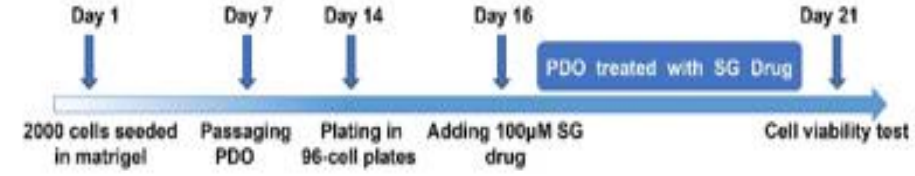

a)

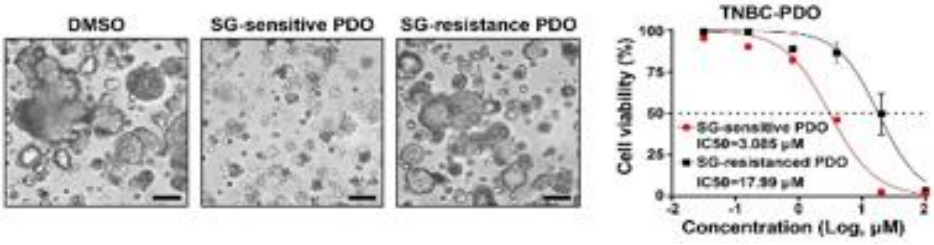

b)

c) d)

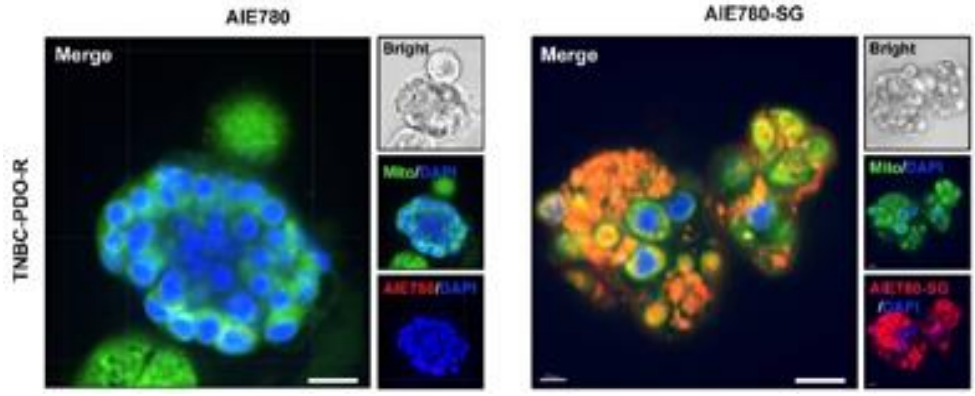

e)

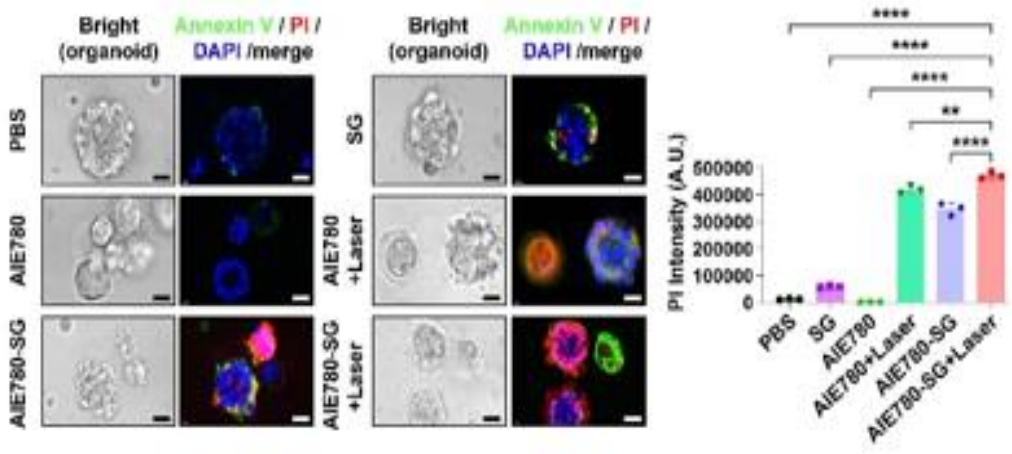

f)

Figure 4. Generation of TNBC organoids and assessment of sensitivity to SG. Confocal micrographs demonstrate targeting by AIE780/AIE780-SG and induction of apoptosis under different treatment conditions.

(a) Overview of the organoid culture workflow and subsequent evaluation of cell viability following SG administration. (b) Bright-field images and corresponding IC50 curves for SG-sensitive and SG-resistant organoids after SG exposure. Scale bar: 100 μm. (c, d) H&E histology and TROP2 immunohistochemical analysis of TNBC PDOs showing prominent TROP2 levels and acquired resistance to SG. Scale bar: 100 μm; 100 μm for the enlarged region. (e) Confocal fluorescence images of SG-resistant TNBC PDOs labeled with red AIE780 or AIE780-SG nanoparticles alongside Mitotracker Green (green). Imaging parameters: AIE780 NPs and AIE780-SG NPs, Ex = 561 nm, Em = 600–700 nm; Mitotracker Green, Ex = 488 nm, Em = 500–565 nm; DAPI (blue), Ex = 405 nm, Em = 410–550 nm. Scale bars: 20 μm. (f) Immunofluorescence detection of apoptosis in TNBC PDOs across treatment groups. PI signal intensity was measured in TNBC PDOs with ImageJ software. Scale bar: 20 μm. PDO, patient-derived organoid; SG, sacituzumab govitecan; TNBC, triple-negative breast cancer; TROP2, trophoblast cell-surface antigen 2. $^{**}p < .01$,$^{****}p < .0001$.

SG exerts its cytotoxic effects primarily through SN-38-dependent inhibition of topoisomerase I, which generates DNA strand breaks, induces cell cycle arrest, and ultimately drives programmed cell death [32]. The integration of photothermal therapy with SG-mediated chemotherapy resulted in substantially amplified tumor cell elimination. Prior reports have noted that BT-20 and MDA-MB-231 cell lines display comparatively reduced responsiveness to IMMU-132 relative to other TNBC lines [33]. Flow cytometry data demonstrated that BT-20 cells receiving the combination of AIE780-SG and laser irradiation underwent markedly higher levels of apoptosis than cells exposed to either SG monotherapy or AIE780 plus laser **(Figure 3d)**. Complementary Western blot results clarified the underlying apoptotic pathway, with evidence of elevated pro-apoptotic protein expression and suppressed BCL-2 levels following photothermal activation of AIE780-SG. In parallel, analysis of damage-associated molecular patterns linked to immunogenic cell death (ICD), such as HMGB1, HSP70, and HSP90 [34], revealed significantly enhanced extracellular release in the AIE780-SG plus laser cohort compared with AIE780 plus laser **(Figure 3e)**. This was accompanied by increased phosphorylation of eIF2-α, an essential mediator in ICD signaling. Surface exposure of calreticulin (ecto-CRT) was also monitored on BT-20 cells. Confocal microscopy showed substantially elevated ecto-CRT presentation in the AIE780-SG plus laser group relative to all other conditions. Quantitative measurements indicated that ecto-CRT fluorescence intensity following illumination of AIE780-SG nanoparticles was roughly 4.6 times greater than that observed with SG treatment alone. Beyond membrane-bound CRT, extracellular ATP concentrations were quantified, revealing markedly higher secretion in the supernatant of cells treated with AIE780-SG plus laser. Collectively, these observations highlight the importance of reactive oxygen species (ROS)-induced mitochondrial dysfunction in promoting tumor immunogenicity [35].

Antitumor activity was further examined by treating TNBC-PDO-R with AIE780-SG and performing Annexin V/PI staining four hours after laser exposure. Quantitative assessment identified a significant elevation in both early apoptotic (Annexin V-positive, green) and necrotic (PI-positive, red) populations, with the highest fraction

of necrotic cells observed in the AIE780-SG plus laser group **(Figure 4f)**. Overall, AIE780-SG nanoparticles exhibit selective accumulation in resistant TNBC-PDO-R models and, when activated by near-infrared light, elicit robust apoptotic and necrotic responses, demonstrating potent therapeutic efficacy within this clinically relevant three-dimensional system.

In vivo biodistribution, tumor suppression capacity, and safety profiling

The use of near-infrared luminescence enables deeper penetration into biological tissues, which is advantageous for noninvasive in vivo imaging [36]. Given its emission characteristics in the NIR-I region, AIE780-SG was advanced for tumor-specific imaging and therapeutic applications. Subcutaneous BT-20 xenografts were developed in mice, followed by systemic intravenous delivery of AIE780-SG or AIE780 at a dose of 12.5 μM (5 μL/g). Real-time infrared thermographic monitoring ensured that tumor temperatures remained below 50°C throughout laser irradiation sessions. Fluorescence-based in vivo tracking showed pronounced and selective accumulation of AIE780-SG within tumor masses, with sharp contrast against surrounding tissues evident by 48 hours. Conversely, plain AIE780 nanoparticles produced negligible fluorescence signals at the tumor site (indicated by red dotted circle) up to 24 hours **(Figure 5a)**. Subsequent ex vivo fluorescence assessment of resected tumors and major organs corroborated the superior tumor-homing properties of AIE780-SG over non-targeted AIE780 **(Figure 5b)**.

After establishing effective in vivo localization and photothermal performance, antitumor activity was investigated in BT-20 xenograft mice assigned to six experimental groups: PBS, SG, AIE780, AIE780 + laser, AIE780-SG, and AIE780-SG + laser. Intratumoral nanoparticle levels peaked at 24 hours following administration. Tumor volumes and animal body weights were measured every two days, with laser applications performed on days 7 and 14. Growth curves and terminal tumor masses revealed only marginal growth retardation in the SG, AIE780, and AIE780 + laser cohorts compared with PBS-treated controls **(Figures 5c and 5d)**. In marked contrast, the AIE780-SG + laser regimen induced dramatic tumor volume reduction, underscoring the synergistic benefits of the combined phototheranostic platform. Histopathological examination at day 21 demonstrated extensive necrotic areas and disrupted cellular architecture in tumor tissues from the AIE780-SG + laser group. Immunohistochemistry further indicated substantially decreased Ki-67 labeling (reflecting lower proliferation) and increased TUNEL staining (indicating enhanced apoptosis) **(Figure 5e)**. These collective observations confirm that NIR-activated AIE780-SG strongly restrains TNBC development by limiting proliferative activity and triggering widespread tumor cell death. In summary, AIE780-SG supports precise NIR-I tumor visualization with prolonged intratumoral residence. When paired with 660 nm laser exposure, it generates powerful photothermal and chemotherapeutic actions that effectively halt TNBC progression through proliferation suppression and apoptosis induction. Biosafety assessment via H&E histology of key organs and serum chemistry analysis (ALB, ALT, ALP, BUN, CREA, UA) revealed no morphological alterations or biochemical abnormalities after 21 days. These results affirm the outstanding biocompatibility of AIE780-SG nanoparticles, positioning them as promising candidates for phototheranostic strategies.

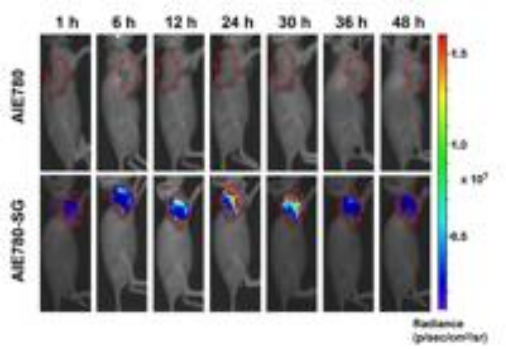

a)

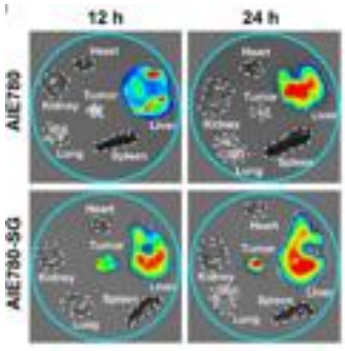

b)

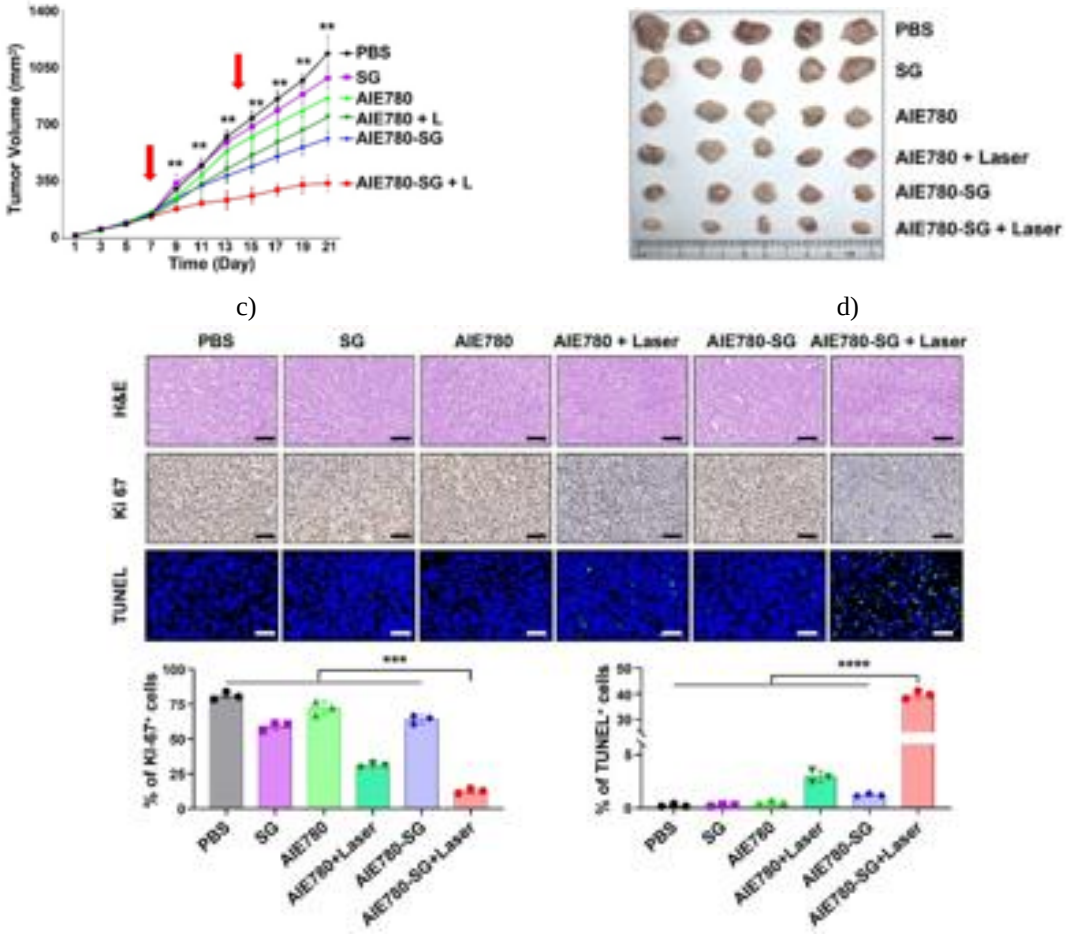

Figure 5. Assessment of in vivo tumor development and therapeutic outcomes following AIE780-SG nanoparticle administration in BT-20 tumor-bearing mice.

(a) Representative in vivo NIR fluorescence images of BT-20 xenograft mice at multiple time points after intravenous administration of AIE780 versus AIE780-SG nanoparticles. Ex = 880 nm, Em = 900 nm. (b) Ex vivo NIR fluorescence images of principal organs and tumors harvested at 12 and 24 h post-intravenous injection of AIE780 or AIE780-SG formulated in PBS. (c) Photographs of excised tumors from nude mice bearing BT-20 xenografts at day 14 after receiving the specified treatments. (d) Quantitative tumor volume progression curves across treatment cohorts. (e) Histopathological and immunohistochemical characterization of tumor sections from groups treated with PBS, sacituzumab govitecan (SG), AIE780, AIE780 + laser, AIE780-SG, and AIE780-SG + laser, evaluated by H&E, Ki67, and TUNEL (green) staining. Scale bar: 100 μm. FLI, fluorescence imaging; NIR, near-infrared; NPs, nanoparticles; PBS, phosphate buffer saline; SG, sacituzumab govitecan. $^{**}p < .01$; $^{***}p < .001$; $^{****}p < .0001$.

Synergistic application of AIE780-SG nanoparticles with photodynamic therapy reduces tumor hypoxia and strengthens NK cell-mediated antitumor responses in vivo

The combination of engineered nanomaterials and phototherapy can reshape the immunosuppressive tumor microenvironment by promoting infiltration of effector immune cells and reducing regulatory populations [37, 38]. Through localized hyperthermia and reactive oxygen species production, such approaches facilitate recruitment of cytotoxic T cells and NK cells into the tumor bed [39]. Aligning with these mechanisms, tumors exposed to AIE780-SG + laser displayed strongly increased MICA/B levels **(Figure 3e)**, which likely contributes to improved NK cell trafficking. CD16 (FcγRIII) functions as a major activating receptor on NK cells capable of directly inducing degranulation following IgG binding [40] It was proposed that surface-presented hRS7 antibody fragments, liberated after nanoparticle internalization, could engage CD16+ NK cells. Specific blockade of CD16 significantly impaired NK cell killing activity in both SG- and AIE780-SG-treated samples and reduced CD107a

degranulation markers, whereas control PBS and AIE780 groups were unaffected. Dendritic cells also support broader antitumor immunity. Analysis of bone marrow-derived dendritic cells by flow cytometry revealed elevated maturation markers (CD80, CD86, and MHC-II) following AIE780-SG + laser exposure **(Figures 6a–6d)**, suggesting enhanced dendritic cell capacity to stimulate NK cells. Accordingly, this group exhibited the largest population of CD49b+ NK cells **(Figure 6e)**. Upon activation, NK cells deploy granzyme B, perforin, and IFN-γ to execute target cell elimination [21, 41]. AIE780-SG + laser treatment increased both NK cell abundance and effector cytokine secretion **(Figure 6f)**. NK cell responsiveness depends on the integrated signaling from various activating receptors such as NKp30, NKp44, NKp46, DNAM-1, and NKG2D [42, 43]. Confocal studies confirmed upregulated expression of NKG2D and CD49b on NK cells within tumors of the AIE780-SG + laser cohort, supporting their augmented killing capability **(Figure 7a)**.

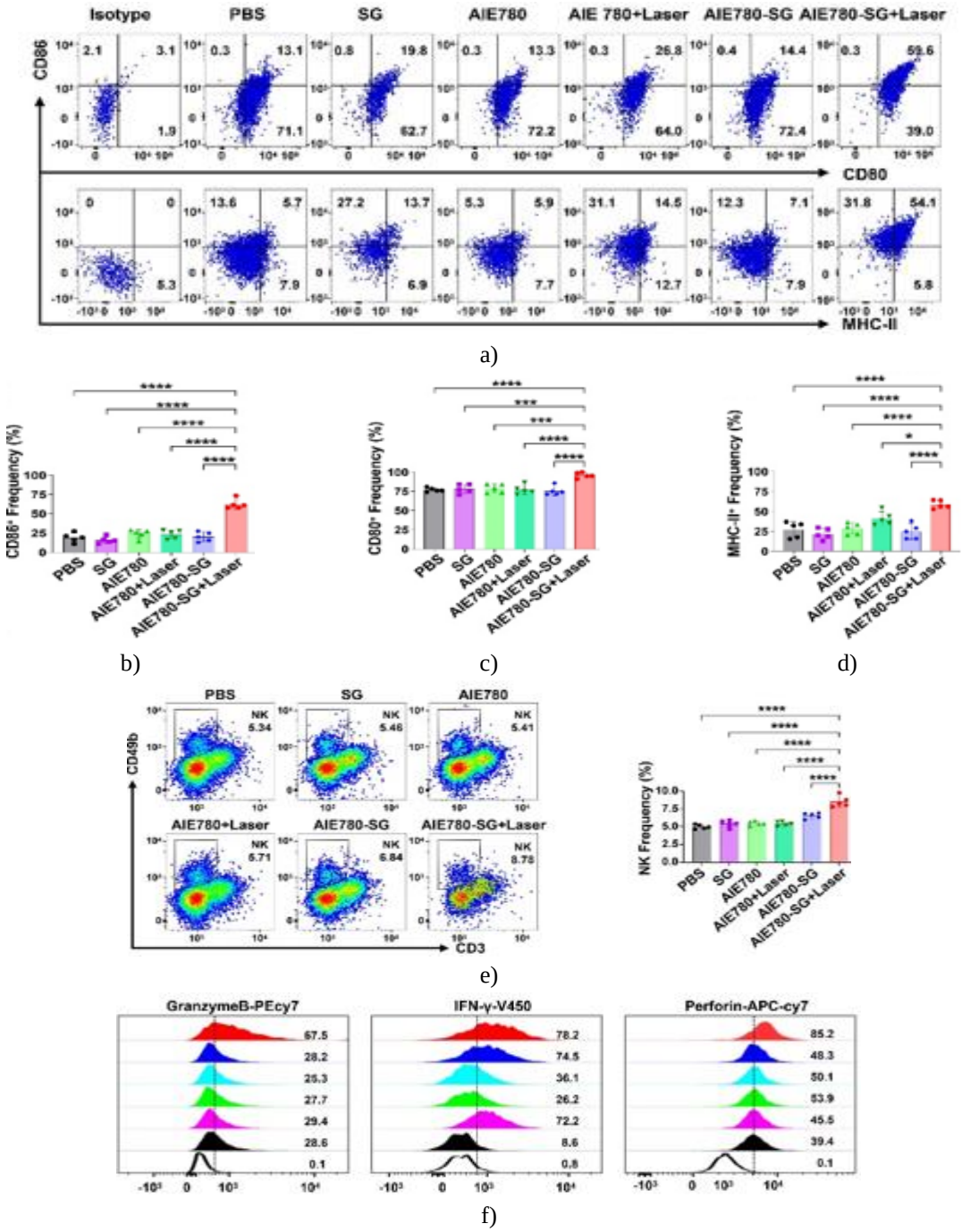

Figure 6. Flow cytometric characterization of cytokine-producing NK cells.
(a) Analysis of surface CD80, CD86, and MHC-II expression by flow cytometry after immunofluorescent labeling in the various treatment conditions. (b–d) Quantitative evaluation of co-expression levels for CD86+,

CD80+, and MHC-II+ following different interventions. (e) Flow cytometry plots and statistical quantification of NK cell populations (CD45+CD3−CD49b+). (f) Proportions of cells positive for Perforin, IFN-γ, and Granzyme B secretion (peak order from bottom to top: Isotype, PBS, SG, AIE780, AIE780 + Laser, AIE780-SG, AIE780-SG + Laser). MHC-II, major histocompatibility complex-II; NK, natural killer; PBS, phosphate buffer saline; SG, sacituzumab govitecan. *p < .05; ***p < .001; ****p < .0001.

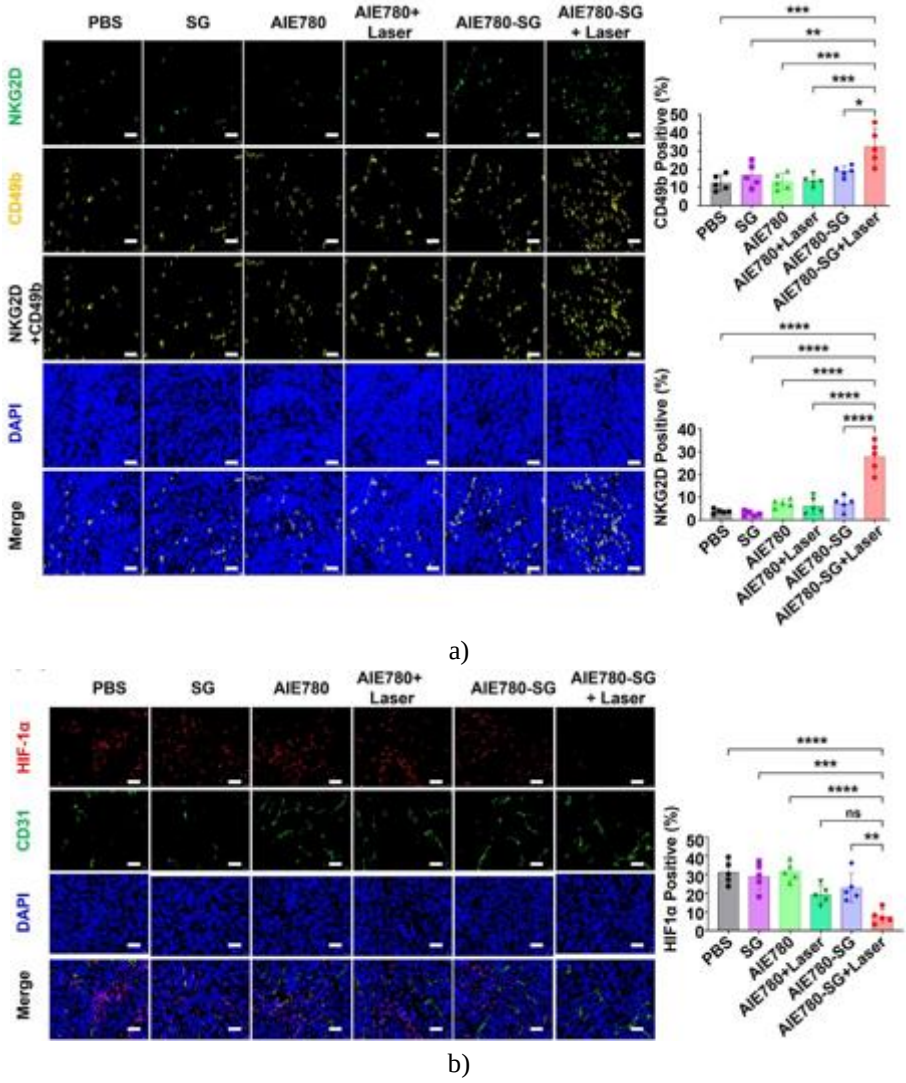

Figure 7. Immunofluorescent evaluation of tumor specimens from mice exposed to distinct treatment protocols.

(a) Detection of CD49b and NKG2D expression with corresponding quantification of positive cell percentages. (b) Immunostaining for CD31, HIF-1α, and DAPI along with quantification of HIF-1α levels. Results are shown as mean ± SD (n = 3), analyzed via one-way ANOVA. Scale bar: 40 μm. Significance levels are indicated as follows: ns, p > .05; *p < .05; **p < .01; ***p < .001; ****p < .0001.

Hypoxic conditions within solid tumors, largely mediated by HIF-1α accumulation in poorly perfused areas [44], limit treatment effectiveness. Oxidative stress and vascular changes induced by photodynamic therapy influence HIF-1α-dependent pathways and associated cell survival signals [45, 46]. Immunohistochemical results indicated that AIE780-SG + laser significantly downregulated HIF-1α while elevating CD31 expression **(Figure 7b)**, consistent with hypoxia relief and favorable vascular reorganization.

This study introduces AIE780-SG nanoparticles as an innovative photoimmunotheranostic system designed to co-deliver the TROP2-directed sacituzumab govitecan (SG) antibody-drug conjugate alongside a mitochondria-

targeted aggregation-induced emission photosensitizer. Leveraging the hRS7 antibody fragment for specific recognition, these nanoparticles demonstrate preferential accumulation in TROP2-overexpressing, SG-resistant triple-negative breast cancer (TNBC) cells and patient-derived organoids. This approach effectively addresses key limitations of conventional SG therapy, including insufficient tumor penetration and rapid systemic clearance. Under 660 nm light irradiation, AIE780 efficiently produces type I reactive oxygen species in mitochondria, resulting in oxidative damage, mitochondrial dysfunction, and immunogenic cell death. Simultaneously, the pH-triggered liberation of SN-38 intensifies DNA lesions and apoptotic signaling, yielding synergistic tumor cell elimination with reduced systemic side effects.

A major obstacle to the long-term success of SG lies in the emergence of acquired resistance, which restricts its therapeutic utility in clinical settings. Multiple pathways contribute to SG resistance, such as (1) variable or diminished TROP2 expression that hinders antibody-drug conjugate binding and internalization; (2) enhanced drug efflux driven by upregulated ATP-binding cassette (ABC) transporters that actively remove SN-38 from malignant cells; and (3) disrupted intracellular transport or lysosomal processing that prevents optimal payload delivery. These adaptations led to substantially reduced SG internalization and attenuated SN-38-mediated DNA damage, as evidenced by decreased γH2AX foci, thereby establishing a complex, multifactorial resistant state. Resistance to TROP2-targeted SG antibody-drug conjugates has been linked to TROP2 downregulation, altered membrane trafficking, and mutations affecting payload targets (e.g., TOP1 inhibitors) [10]. Analogous mechanisms in HER2-directed conjugates such as T-DM1 include antibody evasion, lysosomal impairment, and multidrug resistance (MDR) pump activity [47-49]. Approaches to circumvent antibody-drug conjugate resistance include the development of next-generation payloads (e.g., exatecan derivatives), refined antigen selection, stabilized linkers, and increased payload potency to improve outcomes in combination regimens [50, 51].

AIE780-SG nanoparticles effectively counteract these resistance mechanisms via multiple synergistic strategies: (1) Improved Targeting and Cellular Uptake. The surface-displayed hRS7 fragment maintains strong binding to TROP2, promoting efficient receptor-mediated endocytosis despite lowered receptor abundance. Uptake experiments demonstrated that SG-resistant cells retained ≥80% internalization of AIE780-SG relative to sensitive parental cells, even after a 40% reduction in TROP2 levels, whereas free SG uptake dropped to only 25%. This enhanced delivery helps overcome partial antigen loss. (2) pH-Sensitive Dual Payload Release. In the acidic environment of endolysosomes, the hydrazone bond undergoes cleavage, enabling simultaneous liberation of SN-38 and the photosensitizer. This coordinated release ensures that mitochondrial reactive oxygen species generation by AIE780 persists even if some SN-38 is expelled by efflux pumps, causing organelle disruption and amplified oxidative stress that exhausts cellular protective mechanisms. Notably, SG-resistant cells exposed to AIE780-SG plus light displayed approximately three-fold higher mitochondrial superoxide levels than those treated with SG alone, resulting in pronounced mitochondrial membrane potential ($\Delta\Psi m$) dissipation and apoptotic activation. (3) Circumvention of Efflux-Dependent Resistance. The photosensitizer component is not recognized by ABC transporters, and its reactive oxygen species-mediated effects operate independently of DNA repair pathways. Through induction of immunogenic cell death via mitochondrial perturbation and calreticulin externalization, AIE780-SG successfully eliminates cells otherwise capable of expelling SN-38. Combined treatment with verapamil, a P-gp inhibitor, produced only limited additional benefit for AIE780-SG, confirming the efflux-independent nature of the phototherapeutic component. (4) Immunogenic Cell Death and Tumor Microenvironment Reprogramming. In addition to direct tumoricidal activity, AIE780-SG-triggered immunogenic cell death promotes the liberation of damage-associated molecular patterns and pro-inflammatory mediators (including ATP and HMGB1), thereby transforming immunologically "cold" SG-resistant tumors into "hot" immunogenic lesions. Upregulation of MICA/B on cancer cells facilitates NK cell engagement through NKG2D interactions, while liberated hRS7 fragments support antibody-dependent cellular cytotoxicity via CD16 on NK cells. This dual immune-stimulating effect was not observed with SG monotherapy, emphasizing the unique immunological advantages conferred by the photodynamic approach.

TROP2-mediated metastasis and therapeutic resistance are closely associated with persistent activation of the TROP2/β-catenin positive feedback circuit. This pathway drives nuclear accumulation of β-catenin, augments transcriptional regulation, and promotes epithelial-mesenchymal transition (EMT) together with extracellular matrix (ECM) reorganization. To counteract these effects, Bruceine D has been identified as an agent capable of interfering with TROP2/β-catenin complex assembly, thereby reversing EMT and ECM abnormalities and restoring therapeutic responsiveness [52]. Although conventional IgG-based antibody-drug conjugates exhibit restricted activity in pancreatic cancer, emerging strategies such as nanobody-drug conjugates (NDCs, for

example HuNb-MMAE) offer improved cellular uptake and more efficient payload delivery [53]. Additionally, approaches directed at TROP2's intracellular domain or the concurrent use of ADCs with cyclin D1 inhibitors may produce synergistic therapeutic benefits [54]. Ultimately, overcoming resistance demands an integrated strategy encompassing refined ADC engineering (such as NDCs or ICD-inducing ADCs), remodeling of the tumor microenvironment, and simultaneous inhibition of downstream survival signals (for instance, β-catenin and cyclin D1) to interrupt critical pro-survival cascades [49].

The present results are consistent with and build upon recent progress in organelle-directed nanotherapeutic platforms. Wang *et al*. engineered a mitochondria-targeted supramolecular antagonist incorporating calreticulin (CRT) that increases cancer cell membrane permeability, promotes CRT externalization, decreases mitochondrial membrane potential, and triggers apoptosis, highlighting its promise as an organelle-specific therapeutic agent [55, 56]. Other investigations have shown that AIEgen-based self-assembled nanoparticles conjugated with anti-PD-L1 antibodies markedly improve the combined benefits of photodynamic therapy and immunotherapy against malignant melanoma, resulting in enhanced tumor control and immune stimulation [57]. Similarly, TB/PTX@RTK micelles delivering chemotherapy and photodynamic therapy in conjunction with anti-PD-L1 antibodies were found to synergistically boost systemic antitumor activity in hepatocellular carcinoma models [58]. Ding *et al*. described multifunctional photoactive aggregates based on AIE properties and cisplatin prodrugs that support sustained near-infrared fluorescence imaging, accompanied by potent reactive oxygen species generation and photothermal conversion, leading to effective synergistic outcomes in bladder cancer [59]. Moreover, the integration of chemotherapy and photodynamic therapy not only exerts direct cytotoxic effects on tumor cells but also stimulates immune responses [60, 61]. For example, IR780-derived homodimers have demonstrated substantial suppression of TNBC tumor growth while amplifying immunological activity through robust recruitment of immune cells within the tumor microenvironment [62]. In distinction from these systems, AIE780-SG achieves comprehensive integration of targeted antibody-drug conjugate delivery, photodynamic therapy, and immunomodulatory functions within one nanoparticle platform, conferring superior performance against SG-resistant TNBC.

The capacity of AIE780-SG nanoparticles to selectively localize to mitochondria and elicit immunogenic cell death not only augments the antitumor activity of SG but also strengthens the overall immunogenicity of the treatment. In the current investigation, these nanoparticles effectively inhibited primary tumor expansion in TNBC models by stimulating immune activation and eliciting systemic antitumor immunity, illustrating the advantages of uniting chemotherapeutic and immunotherapeutic modalities in a unified nanomedicine. Nevertheless, several aspects require additional examination. First, detailed pharmacokinetic profiling and extended safety assessments of AIE780-SG should be conducted in larger immunocompetent animal models. Second, although the study emphasized mitochondrial apoptosis, contributions from alternative programmed cell death routes—such as ferroptosis or necroptosis—warrant further exploration. Third, potential synergies between AIE780-SG and immune checkpoint blockade agents (e.g., anti–PD-1/PD-L1 antibodies) could amplify antitumor immunity and promote long-term immunological memory.

In summary, AIE780-SG nanoparticles offer a multifaceted theranostic platform for managing SG-resistant TNBC by integrating precision ADC delivery with photodynamic induction of immunogenic cell death. This combination effectively overcomes chemoresistance and enhances NK cell-driven immune responses. With continued optimization and strategic combinations, this dual-action nanoplatform exhibits considerable promise for clinical development, providing an advanced framework for personalized photoimmunotherapy in challenging breast cancer subtypes.

Conclusion

In conclusion, AIE780-SG nanomedicine constitutes a significant advancement toward improved management of SG-resistant triple-negative breast cancer. Through the coordinated application of photodynamic and chemotherapeutic mechanisms coupled with immune stimulation, this platform holds strong potential to improve treatment responses and deliver a more efficacious multimodal therapeutic strategy for affected patients. Subsequent research should prioritize refinement of the nanoparticles' pharmacological characteristics and their evaluation in clinical contexts, aiming to enhance patient prognosis and expand the utility of immunogenic approaches in cancer therapy.

Acknowledgments: None

Conflict of Interest: None

Financial Support: None

Ethics Statement: None

References

1. Siegel RL, Giaquinto AN, Jemal A. Cancer statistics, 2024. CA Cancer J Clin. 2024;74(1):12-49. doi:10.3322/caac.21820
2. Kim J, Harper A, McCormack V, Sung H, Houssami N, Morgan E, et al. Global patterns and trends in breast cancer incidence and mortality across 185 countries. Nat Med. 2025;31:1154-62.
3. GBD 2021 Diseases and Injuries Collaborators. Global incidence, prevalence, years lived with disability (YLDs), disability-adjusted life-years (DALYs), and healthy life expectancy (HALE) for 371 diseases and injuries in 204 countries and territories and 811 subnational locations, 1990-2021: A systematic analysis for the Global Burden of Disease Study 2021. Lancet. 2024;403(10440):2133-61. doi:10.1016/S0140-6736(24)00757-8
4. Onkar SS, Carleton NM, Lucas PC, Bruno TC, Lee AV, Vignali DAA, et al. The great immune escape: Understanding the divergent immune response in breast cancer subtypes. Cancer Discov. 2023;13(1):23-40.
5. Derakhshan F, Reis-Filho JS. Pathogenesis of triple-negative breast cancer. Annu Rev Pathol. 2022;17:181-204. doi:10.1146/annurev-pathol-042420-093238
6. Nagayama A, Vidula N, Ellisen L, Bardia A. Novel antibody-drug conjugates for triple negative breast cancer. Ther Adv Med Oncol. 2020;12:1758835920915980. doi:10.1177/1758835920915980
7. Bardia A, Hurvitz SA, Tolaney SM, Loirat D, Punie K, Oliveira M, et al. Sacituzumab govitecan in metastatic triple-negative breast cancer. N Engl J Med. 2021;384(16):1529-41. doi:10.1056/NEJMoa2028485
8. Syed YY. Sacituzumab govitecan: First approval. Drugs. 2020;80:1019-25.
9. Jiang Z, Li J, Chen J, Liu Y, Wang K, Nie J, et al. Chinese Society of Clinical Oncology (CSCO) breast cancer guidelines 2022. Transl Breast Cancer Res. 2022;3:13. doi:10.21037/tbcr-22-21
10. Coates JT, Sun S, Leshchiner I, Thimmiah N, Martin EE, McLoughlin D, et al. Parallel genomic alterations of antigen and payload targets mediate polyclonal acquired clinical resistance to sacituzumab govitecan in triple-negative breast cancer. Cancer Discov. 2021;11(10):2436-45. doi:10.1158/2159-8290.CD-21-0702
11. Liu XL, Dong X, Yang SC, Lai X, Liu HJ, Gao Y, et al. Biomimetic liposomal nanoplatinum for targeted cancer chemophototherapy. Adv Sci. 2021;8:2003679. doi:10.1002/advs.202003679
12. Liao Y, Peng Z, Liu X, Hu Y, Zhang J. Theranostic applications of biomolecule-responsive AIEgens. Interdiscip Med. 2023;1:e12065. doi:10.1002/inmd.12065
13. Jin T, Cheng D, Jiang G, Xing W, Liu P, Wang B, et al. Engineering naphthalimide-cyanine integrated near-infrared dye into ROS-responsive nanohybrids for tumor PDT/PTT/chemotherapy. Bioact Mater. 2022;14:42-51. doi:10.1016/j.bioactmat.2021.12.009
14. Wang N, Zhao Z, Xiao X, Mo L, Yao W, Yang H, et al. ROS-responsive self-activatable photosensitizing agent for photodynamic-immunotherapy of cancer. Acta Biomater. 2023;164:511-21. doi:10.1016/j.actbio.2023.03.038
15. Luo J, Xie Z, Lam JWY, Cheng L, Chen H, Qiu C, et al. Aggregation-induced emission of 1-methyl-1,2,3,4,5-pentaphenylsilole. Chem Commun. 2001;37(18):1740-1. doi:10.1039/B105159H
16. Ahmed A, Tait SWG. Targeting immunogenic cell death in cancer. Mol Oncol. 2020;14(12):2994-3006. doi:10.1002/1878-0261.12851
17. Kroemer G, Galassi C, Zitvogel L, Galluzzi L. Immunogenic cell stress and death. Nat Immunol. 2022;23:487-500.
18. Song X, Zhou Z, Li H, Xue Y, Lu X, Bahar I, et al. Pharmacologic suppression of B7-H4 glycosylation restores antitumor immunity in immune-cold breast cancers. Cancer Discov. 2020;10(12):1872-93. doi:10.1158/2159-8290.CD-20-0402

19. Qian X, Yang H, Ye Z, Gao B, Qian Z, Ding Y, et al. Celecoxib augments paclitaxel-induced immunogenic cell death in triple-negative breast cancer. ACS Nano. 2024;18(24):15864-77. doi:10.1021/acsnano.4c02947
20. Cullen JK, Yap PY, Ferguson B, Bruce ZC, Koyama M, Handoko H, et al. Tigilanol tiglate is an oncolytic small molecule that induces immunogenic cell death and enhances the response of both target and non-injected tumors to immune checkpoint blockade. J Immunother Cancer. 2024;12(4):e006602. doi:10.1136/jitc-2022-006602
21. Zhang L, Chen X, Zhou B, Meng W, Zeng H, Chen Y, et al. Cocktail strategy-based nanomedicine: A synergistic cascade of starvation, NIR-II photothermal, and gas therapy for enhanced tumor immunotherapy. Acta Biomater. 2025;193:316-33.
22. Obeid M, Tesniere A, Ghiringhelli F, Fimia GM, Apetoh L, Perfettini JL, et al. Calreticulin exposure dictates the immunogenicity of cancer cell death. Nat Med. 2007;13(1):54-61. doi:10.1038/nm1523
23. Lin H, Kryczek I, Li S, Green MD, Ali A, Hamasha R, et al. Stanniocalcin 1 is a phagocytosis checkpoint driving tumor immune resistance. Cancer Cell. 2021;39(4):480-93.e6. doi:10.1016/j.ccell.2020.12.023
24. Yu Y, Wu S, Zhang L, Xu S, Dai C, Gan S, et al. Cationization to boost both type I and type II ROS generation for photodynamic therapy. Biomaterials. 2022;280:121255.
25. Dekkers JF, van Vliet EJ, Sachs N, Rosenbluth JM, Kopper O, Rebel HG, et al. Long-term culture, genetic manipulation and xenotransplantation of human normal and breast cancer organoids. Nat Protoc. 2021;16:1936-65.
26. Liu H, Su J. Organoid and organoid extracellular vesicles for osteoporotic fractures therapy: Current status and future perspectives. Interdiscip Med. 2023;1:e20230011. doi:10.1002/inmd.20230011
27. Gong Z, Hou D, Xu Y, Wang M, Lin S, Zheng Y, et al. Enhancing SDT efficacy of doxorubicin-loaded sonosensitizer micelles to overcome resistance of cancer therapy by optimizing acoustic parameters. Aggregate. 2025;6:e70005. doi:10.1002/agt2.70005
28. Chen Q, Liu Z. Albumin carriers for cancer theranostics: A conventional platform with new promise. Adv Mater. 2016;28(47):10557-66. doi:10.1002/adma.201600038
29. Zhang L, Li CX, Wan SS, Zhang XZ. Nanocatalyst-mediated chemodynamic tumor therapy. Adv Healthc Mater. 2022;11(2):e2101971. doi:10.1002/adhm.202101971
30. Ding T, Wang S, Zhang X, Zai W, Fan J, Chen W, et al. Kidney protection effects of dihydroquercetin on diabetic nephropathy through suppressing ROS and NLRP3 inflammasome. Phytomedicine. 2018;41:45-53. doi:10.1016/j.phymed.2018.01.026
31. Bonner WM, Redon CE, Dickey JS, Nakamura AJ, Sedelnikova OA, Solier S, et al. GammaH2AX and cancer. Nat Rev Cancer. 2008;8(12):957-67. doi:10.1038/nrc2523
32. Rugo HS, Bardia A, Marme F, Cortés J, Schmid P, Loirat D, et al. Overall survival with sacituzumab govitecan in hormone receptor-positive and human epidermal growth factor receptor 2-negative metastatic breast cancer (TROPiCS-02): A randomised, open-label, multicentre, phase 3 trial. Lancet. 2023;402(10411):1423-33. doi:10.1016/S0140-6736(23)01245-X
33. Cardillo TM, Sharkey RM, Rossi DL, Arrojo R, Mostafa AA, Goldenberg DM. Synthetic lethality exploitation by an anti-Trop-2-SN-38 antibody-drug conjugate, IMMU-132, plus PARP inhibitors in BRCA1/2-wild-type triple-negative breast cancer. Clin Cancer Res. 2017;23(13):3405-15. doi:10.1158/1078-0432.CCR-16-2401
34. Du S, Zhang X, Jia Y, Peng P, Kong Q, Jiang S, et al. Hepatocyte HSPA12A inhibits macrophage chemotaxis and activation to attenuate liver ischemia/reperfusion injury via suppressing glycolysis-mediated HMGB1 lactylation and secretion of hepatocytes. Theranostics. 2023;13(11):3856-71. doi:10.7150/thno.82607
35. Kepp O, Semeraro M, Bravo-San Pedro JM, Bloy N, Buqué A, Huang X, et al. eIF2α phosphorylation as a biomarker of immunogenic cell death. Semin Cancer Biol. 2015;33:86-92. doi:10.1016/j.semcancer.2015.02.004
36. Yang Y, Jiang Q, Zhang F. Nanocrystals for deep-tissue in vivo luminescence imaging in the near-infrared region. Chem Rev. 2024;124(2):554-628. doi:10.1021/acs.chemrev.3c00506
37. Dai J, Fang L, Wang X, Hua J, Tu Y, Li S, et al. Configuration-mediated efficient non-radiative transition for R848-assisted photothermal immunotherapy to inhibit tumor growth and metastasis by an in situ tumor vaccine strategy. Angew Chem Int Ed. 2025;64:e202417871. doi:10.1002/anie.202417871

38. Qi MH, Wang DD, Qian W, Zhang ZL, Ao YW, Li JM, et al. High-efficiency gold nanoaggregates for NIR LED-driven sustained mild photothermal therapy achieving complete tumor eradication and immune enhancement. Adv Mater. 2025;37:2412191. doi:10.1002/adma.202412191
39. Han S, Wang W, Wang S, Yang T, Zhang G, Wang D, et al. Tumor microenvironment remodeling and tumor therapy based on M2-like tumor associated macrophage-targeting nano-complexes. Theranostics. 2021;11(6):2892-916. doi:10.7150/thno.50928
40. Crinier A, Narni-Mancinelli E, Ugolini S, Vivier E. SnapShot: Natural killer cells. Cell. 2020;180(6):1280.e1. doi:10.1016/j.cell.2020.02.029
41. Myers JA, Miller JS. Exploring the NK cell platform for cancer immunotherapy. Nat Rev Clin Oncol. 2021;18:85-100.
42. Morvan MG, Lanier LL. NK cells and cancer: You can teach innate cells new tricks. Nat Rev Cancer. 2016;16:7-19.
43. Liang C, Ding X, Li X, Jiang X, Yang H, Yang H, et al. In situ self-reassembling nanosystem enhances PD-L1 blockade for cancer immunotherapy. J Control Release. 2025;377:767-80.
44. de Heer EC, Jalving M, Harris AL. HIFs, angiogenesis, and metabolism: Elusive enemies in breast cancer. J Clin Invest. 2020;130(10):5074-87. doi:10.1172/JCI137552
45. Agostinis P, Berg K, Cengel KA, Foster TH, Girotti AW, Gollnick SO, et al. Photodynamic therapy of cancer: An update. CA Cancer J Clin. 2011;61(4):250-81. doi:10.3322/caac.20114
46. Ma S, Wang F, Dong J, Wang N, Tao S, Du J, et al. Inhibition of hypoxia-inducible factor 1 by acriflavine renders glioblastoma sensitive for photodynamic therapy. J Photochem Photobiol B. 2022;234:112537. doi:10.1016/j.jphotobiol.2022.112537
47. Chen YF, Xu YY, Shao ZM, Yu KD. Resistance to antibody-drug conjugates in breast cancer: Mechanisms and solutions. Cancer Commun (Lond). 2023;43(3):297-337. doi:10.1002/cac2.12387
48. Ríos-Luci C, García-Alonso S, Díaz-Rodríguez E, Nadal-Serrano M, Arribas J, Ocaña A, et al. Resistance to the antibody-drug conjugate T-DM1 is based in a reduction in lysosomal proteolytic activity. Cancer Res. 2017;77(17):4639-51. doi:10.1158/0008-5472.CAN-16-3127
49. Weng W, Meng T, Zhao Q, Shen Y, Fu G, Shi J, et al. Antibody-exatecan conjugates with a novel self-immolative moiety overcome resistance in colon and lung cancer. Cancer Discov. 2023;13(4):950-73. doi:10.1158/2159-8290.CD-22-1368
50. Liu H, Zeng H, Qin X, Ning W, Xu L, Yang S, et al. The Icarian flight of antibody-drug conjugates: Target selection amidst complexity and tackling adverse impacts. Protein Cell. 2025;16(7):532-56. doi:10.1093/procel/pwaf002
51. Boghaert ER, Cox MC, Vaidya KS. Pathophysiologic and pharmacologic considerations to improve the design and application of antibody-drug conjugates. Cancer Res. 2022;82(10):1858-69. doi:10.1158/0008-5472.CAN-21-3236
52. Tang W, Hu Y, Tu K, Gong Z, Zhu M, Yang T, et al. Targeting Trop2 by Bruceine D suppresses breast cancer metastasis by blocking Trop2/β-catenin positive feedback loop. J Adv Res. 2024;58:193-210. doi:10.1016/j.jare.2023.05.012
53. Xu C, Zhu M, Wang Q, Cui J, Huang Y, Huang X, et al. TROP2-directed nanobody-drug conjugate elicited potent antitumor effect in pancreatic cancer. J Nanobiotechnol. 2023;21(1):410. doi:10.1186/s12951-023-02183-9
54. Ju X, Jiao X, Ertel A, Casimiro MC, Di Sante G, Deng S, et al. V-Src oncogene induces Trop2 proteolytic activation via cyclin D1. Cancer Res. 2016;76(22):6723-34. doi:10.1158/0008-5472.CAN-15-3327
55. Nishida K, Sekida S, Anada T, Tanaka M. Modulation of biological responses of tumor cells adhered to poly(2-methoxyethyl acrylate) with increasing cell viability under serum-free conditions. ACS Biomater Sci Eng. 2022;8(2):672-81. doi:10.1021/acsbiomaterials.1c01469
56. Wang Y, Zhan J, Huang J, Wang X, Chen Z, Yang Z, et al. Dynamic responsiveness of self-assembling peptide-based nano-drug systems. Interdiscip Med. 2023;1:e20220005. doi:10.1002/inmd.20220005
57. Li L, Xu Q, Zhang X, Jiang Y, Zhang L, Guo J, et al. AIEgen-self-assembled nanoparticles with anti-PD-L1 antibody functionalization realize enhanced synergistic photodynamic therapy and immunotherapy against malignant melanoma. Mater Today Bio. 2025;30:101387.

58. Xu J, Zheng Q, Cheng X, Hu S, Zhang C, Zhou X, et al. Chemo-photodynamic therapy with light-triggered disassembly of theranostic nanoplatform in combination with checkpoint blockade for immunotherapy of hepatocellular carcinoma. J Nanobiotechnol. 2021;19(1):355. doi:10.1186/s12951-021-01101-1
59. Ding K, Wang L, Zhu J, He D, Huang Y, Zhang W, et al. Photo-enhanced chemotherapy performance in bladder cancer treatment via albumin coated AIE aggregates. ACS Nano. 2022;16(5):7535-46. doi:10.1021/acsnano.1c10770
60. Liu X, Huang J, Zhou H, Wang S, Guo X, Mao J, et al. Inhibition of PDT-induced PGE2 surge for enhanced photo-immunotherapy. Biomaterials. 2025;317:123116. doi:10.1016/j.biomaterials.2025.123116
61. Zhang T, Tang D, Wu P, Jiang S, Zhang Y, Naeem A, et al. NIR-II photo-accelerated polymer nanoparticles boost tumor immunotherapy via PD-L1 silencing and immunogenic cell death. Bioact Mater. 2025;46:285-300.
62. Xue Y, Chen K, Chen Y, Liu Y, Tang J, Zhang X, et al. Engineering diselenide-IR780 homodimeric nanoassemblies with enhanced photodynamic and immunotherapeutic effects for triple-negative breast cancer treatment. ACS Nano. 2023;17(22):22553-70.